Chapter 7
Characterization techniques for studying the properties of nanocarriers for systemic delivery

Aditi Mehta[1*], Olivia M. Merkel[1]*

1. Department of Pharmacy, Pharmaceutical Technology and Biopharmaceutics, Ludwig-Maximilian University of Munich, Butenandtstr. 5-13, 81377 Munich, Germany

* Email: Olivia.merkel@lmu.de (OMM) and aditi.mehta@cup.uni-muenchen.de (AM)

Abstract
Nanocarriers have attracted a huge interest in the last decade as efficient drug delivery systems and diagnostic tools. They enable effective, targeted, controlled delivery of therapeutic molecules while lowering the side effects caused during the treatment. The physicochemical properties of nanoparticles determine their *in vivo* pharmacokinetics, biodistribution and tolerability. The most analyzed among these physicochemical properties are shape, size, surface charge and porosity and several techniques have been used to characterize these specific properties. These different techniques assess the particles under varying conditions, such as physical state, solvents etc. and as such probe, in addition to the particles themselves, artifacts due to sample preparation or environment during measurement. Here, we discuss the different methods to precisely evaluate these properties, including their advantages or disadvantages. In several cases, there are physical properties that can be evaluated by more than one technique. Different strengths and limitations of each technique complicate the choice of the most suitable method, while often a combinatorial characterization approach is needed.

Keywords
nanoparticle characterization, nanoparticles, porosity, shape, size, surface charge

7.1 Introduction
Nanomaterials are generally defined as materials wherein '*50 % or more of the particles in the number size distribution, one or more external dimensions is in the size range 1 nm - 100 nm*' [1] and are important components in novel drug formulation. Due to their small size and large surface area, nanoparticles can help increase solubility and thus enhanced bioavailability, can mediate additional ability to cross the blood brain barrier (BBB), enter the pulmonary system and be absorbed through the tight junctions of endothelial cells of the skin [2]. Carriers used in drug delivery systems are made of polymers (polymeric carriers, matrices, micelles or dendrimers), lipids (liposomes or solid lipid carriers), gold carriers, viruses, nanotubes and magnetic carriers (Figure 1) [3]. They have been shown to efficiently transport therapeutic agents to cells influencing the pharmacokinetics of transport, drug release and distribution of the active drug. The advantages of using nanocarriers include increased bioavailability of the drug, protection against degradation and stabilization of more sensitive agents (e.g. proteins, antibodies),

resulting in their higher concentrations in the target tissue and reduced side effects [4]. Moreover, nanocarriers can be attached to targeting ligands [5], [6], [7] such that their specificity to target cells/tissues can be increased. In addition, nanocarriers can also be used to deliver hydrophobic or poorly water-soluble drugs, for instance by using micelles which assemble into a hydrophobic core and hydrophilic shell. A remarkable example is Doxil®. The first FDA approved nano-drug composes the drug doxorubicin loaded within PEGylated nano-liposomes, which demonstrates prolonged drug circulation time and avoids clearance by the reticuloendothelial system (RES). Nanocarriers also allow for synergistic therapy options via the codelivery of multiple drugs at the same time to the same location with the same pharmacokinetics.

Over the last several decades, nanocarriers have become an attractive option to deliver therapeutic molecules to target tissues after systemic delivery. However, the physical and chemical properties of nanocarriers affect their biodistribution and tissue retention within the body [8], [9]. Nanocarriers can be administered either by direct injection, inhalation or via oral intake. Once they are part of the systemic circulation, they interact with serum proteins [10], adsorb small molecules, such as amino acids, folate, biotin and many others [11]. Specifically, their shape and size strongly influences cellular uptake. It has been shown that 100 nm particles exhibited a 2.5-fold greater uptake compared to 1 μm diameter particles *in vitro* [12]. Another challenge to these nanoparticles is the immune system. While small particles (<30 nm) are rapidly cleared by the kidney, while those >30 nm in size are cleared by the reticuloendothelial system (RES), including macrophages in the liver and spleen. Whether nanocarriers are taken up by macrophages or not, depends on opsonization by the innate immune system [13]. On the other hand, the size and surface properties of the nanoparticles also influences their *in vivo* stability [14]. For instance, PEGylation, i.e. conjugation of a polymer polyethylene glycol (PEG, $(CH_2CH_2O)_n$) on the nanoparticle surface can at least partially protect them from opsonization [15].

In fact, nanoparticle size in particular affects immune cell sequestration and subsequent clearance from the blood stream. It was observed that particles greater than 200 nm activate the lymphatic system and are removed from circulation quicker [16]. Moreoever, nanoparticle size considerably influences its cytotoxicity. Xiong et al. demonstrated size dependent cytotoxicity, with smaller (60 – 100nm) particles triggering more damage, as measured by the release of TNF- α as compared to those above 200nm [17]. For systemically delivered nanocarriers, the nanocarriers-drug complexes should also remain soluble and stable, escape aggregation in the blood, or prevent exposure of their 'cargo' to degrading enzymes within the blood or inter-tissue fluid. Determining the physicochemical properties of nanoparticles and exploring their structure-function-interaction relationships is, therefore, a critical part of nanomedicine. Characterization parameters, *shape, size, surface charge, porosity* and *viscosity,* and the different characterization techniques, each based on different physical properties, are described in this chapter.

7.2 Shape and size distribution

As discussed above, the shape and size of nanocarriers are the most important and most studied parameters in their characterization, influencing their size distribution, degree of aggregation, surface charge and area as well as *in vivo* biodistribution, tolerability as well as pharmacokinetics. Moreover, due to the synthesis process of nanocarriers, the product is often prone to be a polydispersion of nanoparticles which sometimes might be of a broad distribution, making size distribution analysis crucial to understanding nanoparticle behaviour *in vivo*. The morphological characterization of nanocarriers can be performed by direct or indirect methods. Direct methods, including for example microscopy, X-ray diffraction and scattering, radioimmunoassay, rely on directly observing the nanocarriers together with the therapeutic material and distinguishing this assembly from its individual components, the carrier and the therapeutic material. On the other hand, indirect techniques focus on the parameters of a suspension or solution containing all three entities, the carrier-therapeutic assembly, the therapeutic material and the carrier alone, thereby remaining unable to identify the differences between the pure components. Indirect methods include for example static and dynamic light scattering, absorbance, linear and circular dichroism, zeta potential.

7.2.1 Transmission electron microscopy

Transmission electron microscopy (TEM) is one of the most efficient tools for nanomaterials characterization. TEM is based on the interaction between a uniform current density electron beam and a thin sample. The extent of this interaction is dependent on the size, sample density and elemental composition of the sample. As the electron beam reaches the sample, the electrons interacting with specimen are transformed to unscattered electrons, elastically scattered electrons or inelastically scattered electrons [18]. The scattered or unscattered electrons are then focused by a series of electromagnetic lenses and projected on a screen to generate an electron diffraction, amplitude-contrast image, a phase-contrast image or a shadow image of varying darkness according to the density of unscattered electrons (Figure 2A) [18].

Both TEM and light microscopes operate on the same basic principle, however, due to the much shorter wavelength of electrons, TEM achieves a much higher level of resolution up to the level of atomic dimensions (<1 nm). Moreover, TEM provides the most accurate estimation of nanoparticle homogeneity. TEM is undoubtedly the most important and frequently used nanoparticle characterization technique.

The abovementioned advantages of TEM are also accompanied by serious limitations. Due to the high resolution provided by TEM, sampling is often challenging, allowing the user to only view a small section of the sample. Another problem of sampling is that for TEM imaging, very thin (electron transparent) specimen are required, and specimens <100 nm in thickness should be used wherever possible. However, the thinning processes used affect the specimens, changing both their structure and chemistry. In addition, due to the high energy, the electron beam can damage organic, polymer and hybrid nanoparticles. This problem can be addressed by either reducing the acceleration of the electron beam (however simultaneously reducing the attained resolution) or using Cryo-TEM (discussed in section 1.4). Another problem is that TEM presents 2D images of 3D

specimens, averaged through the thickness of the sample, thereby lacking depth sensitivity, also known as 'projection-limitation' [18].

7.2.2 Scanning electron microscopy

In scanning electron microscopy (SEM) a focused beam of high-energy electrons is incident across a sample in a raster pattern. The emitted electrons are detected by a detector for each position in the scanned area, generating an image by the interaction signals obtained at the surface of solid samples (Figure 2B). The intensity of the emitted electron signal is displayed as brightness on a display monitor and is stored in a digital image file that represents the morphology of the sample surface. Since SEM uses electron beams that are less powerful than for TEM, it limits their penetration depth and therefore, the results are sensitive to the surface morphology, with the advantage of minimal to no damage to the sample. However, due to the low energy electron beams, the resolution limit of SEM is typically around 3 nm. While SEM only yields information on the sample surface structure, TEM interacts with the whole sample volume, thereby providing information on the sample's internal structures. A direct comparison of SEM and TEM for the same nanoparticles was described by He and colleagues confirming these observations (Figure 2C-D) [19].

Although sample preparation for SEM is straightforward and simple, the samples are dried and imaged under vacuum, which may alter the topography of the sample. In addition, for high resolution imaging, the samples are required to be conductive. Non-conductive samples need to be coated by a thin layer (<10 nm) of a metallic film before being analysed. An alternative method, **environmental or wet SEM**, is performed at low pressure instead of high vacuum and allows the analysis of hydrated materials without fixing, drying or coating of the specimen [20]. However, environmental SEM has a lower spatial resolution than standard SEM imaging and has so far been limited to the characterization of microspheres and microcapsules [17].

SEM can be operated in the transmission mode, i.e. through the technique called 'scanning-transmission electron microscopy' (STEM), which combines both operational modes, SEM and TEM. In STEM mode, a convergent electron beam is focused to a small area of the sample. To register an image, the electron probe is raster-scanned and subsequently propagated through the sample. Due to the electron-matter interaction, the trajectory of the electrons is scattered away and different kinds of signals are registered in sync with the electron probe scanning. Using STEM, advanced nanoparticle analysis can be carried out in the transmission mode by gaining in-depth information, and analysis of ensembles of particles is possible [21]. One of the main advantages of STEM over TEM is that the electrons scattered out to high angles on a high-angle annular dark field detector (HAADF) are chemically sensitive, and a sample with a definite crystalline arrangement is not a requirement.

7.2.3 Cryo-TEM

Cryo-TEM was developed in the 1980s to visualize biological samples in their vitrified, frozen-hydrated state, i.e. in a near native state at the resolution of TEM (0.1–2 nm). Although originally developed to image biological samples in water, Cryo-TEM

currently plays an important role in visualizing viruses [22], lipids- and polymer-based nanocarriers [23], [24] validating the structural integrity of nanoparticles. Cryo-TEM can be applied to samples in organic solvents or in aqueous surroundings, thereby allowing the visualization of nanoparticles under different solvent conditions as well as evaluate the changes during the development or self-assembly of the particles.

Typically, in Cryo-TEM, samples are suspended in a thin layer of frozen buffer stretched across a carbon grid in a specialized holder, which also contains a small dewar for liquid nitrogen as cooling agent at its end. Adequate sample cooling is essential to avoid sample damage by freeze drying. In Cryo-TEM, the frozen sample grid is kept at liquid nitrogen temperature during imaging in a TEM, thereby taking images of the sample in its frozen but hydrated state. Since the sample is flash frozen, Cryo-TEM avoids artefacts that result from sample drying.

Currently, Cryo-TEM is considered the gold standard for liposome imaging [25]. An interesting recent example is the imaging and characterization of a widely used anticancer agents, namely doxorubicin encapsulated in liposomes. In 2016, Wibroe et al. assessed liposome morphology of four liposomal doxorubicin formulations, Doxil®, Caelyx®, DOXOrubicin and SinaDoxosome (Figure 3) [26]. They observed that while Doxil, Caelyx and DOXOrubicin show intact spherical and prolate ellipsoidal unilamellar vesicles, SinaDoxosome, revealed co-existence of flat circular disks along with unilamellar vesicles.

Despite its many advantages over traditional TEM, Cryo-TEM also suffers some drawbacks. A significant concern of Cryo-TEM is that since the samples are frozen, the density difference between the sample and the frozen water is minimal resulting in a reduced contrast obtained in micrographs. To circumvent this problem, often Cryo-TEM micrographs are taken a few micrometers out of focus to generate phase contrast in the image [27]. In addition, frozen samples are more sensitive to electron damage and can only tolerate lower electron doses, approximately 10^3 fold lower than in TEM, before significant damage occurs to the samples.

Cryo-TEM images provide useful information about the shape, size and importantly, the integrity of the nanoparticles. Furthermore, Cryo-TEM can also be used to determine 3D structures of nanocarriers at atomic resolution. For structurally and chemically homogenous particles, such as icosahedral viral vectors, protein based nanoparticles [28] or gold nanoparticles [29], single particle reconstruction may be performed by averaging multiple Cryo-TEM micrographs taken in various orientations. On the other hand, for irregularly shaped or heterogenous nanocarriers, such as liposomes or multipolymer micelles [30], Cryo-electron tomography (Cryo-ET) may be performed, wherein the sample is tilted through a large angular range (for instance, -80° to +80°) collecting a tilt series of images of a single specimen area. The electron dose is a critical factor, especially for Cryo-ET images, and should be maintained at approximately 20 electrons/Å^2. Irrespective of the method used, 3D reconstructions provide a complete representation of the sample as well as spatially accurate and quantitative measurements of each sample.

7.2.4 Atomic Force Microscopy

Atomic force microscopy (AFM) belongs to the family of scanning probe microscopy (SPM) techniques and was developed in 1985 combining the principles of scanning tunneling microscopy and the stylus profilometer [31]. AFM uses a sharp tip probe at the end of a cantilever of a probe to scan the surface properties of the specimen. AFM can be used to assess surface properties, such as morphology and mechanical properties of materials at an exceptionally high (nanometer) resolution [31]. This high resolution of AFM is achieved due to a combination of its probe (normally a sharp tip), carefully controlled tip-specimen forces, the optical level and high-precision movement of the scanner. The probe is generally less than 5μm in length and 10 nm in diameter at the apex and is located at the end of a microscale cantilever which is 100-500 μm long (Figure 4A, B) [32]. This tip moves over the sample surfaces and due to the tip-surface attractive or repulsive forces, the cantilever moves vertically, and a laser beam focussed on the back of the cantilever is deflected and detected. Therefore, the movement of the tip can be monitored by alterations in the laser which is then ultimately translated into a 3D image. A piezoelectric scanner is used to precisely control the probe - sample position and the accurate movement of the probe tip over the sample surface [33],[31]. AFM permits quantitative, high-resolution, non-destructive imaging of surfaces, including biological ones.

AFM allows shape and size measurements of nanocarriers under different conditions, such as various charge ratios, pH ranges and salt concentrations, without any special treatment or vacuum conditions [33]. AFM can be operated in different modes, of which the two most popular are the contact and non-contact mode. In the contact mode, as implied by the name, the AFM tip is in contact with the sample surface. As the scanner moves over the sample surface, the cantilever deflection is sensitive to changes in surface topography [33]. In this case, the interaction between the tip and the sample is repulsive and coupled to the frictional force; it can damage softer samples and is therefore ideal for imaging relatively hard samples [34].

In the non-contact mode, the cantilever is oscillated above the sample surface (5-15 nm above, amplitude < 10 nm) near its resonant frequency (100 – 400 kHz). The attractive forces between the tip and surface change according to the distance between them, which induce alterations in the resonant behaviour of the oscillating cantilever. These changes in frequency or phase and amplitude are used to generate images. The main advantage of the non-contact mode is that the tip never comes in contact with the sample and therefore the sample remains undisturbed making it suitable for soft or vulnerable samples, such as biological samples.

An intermediate and the most commonly used mode is the tapping mode, wherein the cantilever is oscillated over the sample and to achieve the highest resolution, comes very close to the sample, often making intermittent contact with the sample. The short contact further dampens the oscillation amplitude which can be further translated to an image. This mode circumvents the lateral forces in the sample while minimizing frictional forces [35], [36]. In the tapping mode, topography and phase images are simultaneously

acquired so as to obtain information on different properties of the sample [37]. The tapping mode is appropriate for samples weakly bound to the surface or soft samples, such as polymers, lipid bilayers, DNA, or proteins. [38], [39], [40].

Common AFM probes include silicon or silicon nitride probes and carbon nanotube tips [41]. The tip, however, can be modified according to different applications. For instance, for micrometer-scale imaging and mechanical testing, spherical tips can be constructed by gluing colloid or glass spheres to the AFM tips [38]. Interestingly, AFM probes can also be functionalized by coating polymers or proteins onto the tips thereby allowing measurements of the force required for the interaction between the substrate and protein/polymer. Using folic acid receptor (FRα) coated cantilevers, Jones et al. demonstrated the interactions between free folic acid or folic acid decorated micelleplex nanoparticles [42]. The nanoparticles investigated in the latter study consisted of micelles formed with a FA conjugated triblock copolymer (PEI-g-PCL-b-PEG-FA) which condensed siRNA to form micelleplexes. Using this modified cantilever, over 1000 force measurements were made for each substrate and the binding probability as well as rupture force was determined (Figure 4C). They demonstrated that the folate decorated micelleplexes had a significantly higher binding force as compared to free folic acid.

7.2.5 X-ray diffraction
X-ray techniques are generally non-destructive and provide information about the ensemble average of many particles, in contrast to direct imaging techniques such as electron microscopy where only a very small sample of particles is analyzed which may not be truly representative of the material, for example, in case of polydisperse particles. X-ray techniques provide direct measures of particle size and lattice dimensions, in contrast to other indirect methods such as UV–visible spectroscopy, where the particle size is inferred from the systematic shift in the position of the absorption peak.

The importance of X-ray diffraction (XRD) was evident soon after its discovery. X-ray diffraction was proposed in 1912 by Max von Laue, who was awarded the Nobel Prize in 1914 for the same. In the next year, father and son William Henry Bragg and William Lawrence Bragg received the Nobel Prize for determining the first crystal structures using X-rays. They characterized the atomic order of sodium chloride and other similar compounds and since then, crystal structures of more and more complex compounds have been elucidated. XRD allows for the determination of the atomic or molecular structures of all types of materials, which is a prerequisite for understanding their properties.

XRD is based on the constructive interference of a crystalline sample and monochromatic X-rays directed toward the sample, generated by a cathode ray tube, filtered to produce monochromatic radiation. The interaction of the incident rays with the sample produces constructive interference (and a diffracted ray) when conditions satisfy Bragg's Law ($n\lambda = 2d \sin \theta$). This law relates the wavelength of electromagnetic radiation to the diffraction angle and the lattice spacing in a crystalline sample. The larger the collection angle (or smaller the wavelength), the higher the achieved data resolution. These diffracted X-rays are then detected, processed and counted. By scanning a sample through a range of angles, all possible diffraction directions of the lattice should be

attained due to the random orientation of the powdered material. XRD provides information about the crystal components, their average shape and size, nature of the phase, lattice parameters and crystalline gain size. For the latter, the Scherrer equation is used by broadening of the most intense peak of an XRD measurement.

XRD is performed in dry, powdered samples, commonly after evaporating their colloidal suspensions. In the area of nanoparticles, X-ray scattering and diffraction allow the non-destructive, direct evaluation of the crystal and particle size and their crystallographic phase. Interestingly, Upadhyay et al. determined the average crystal size of magnetite nanoparticles in the range of 9-53 nm. However, the TEM deduced size of the same was found to be higher than that calculated from XRD. They further showed that when the particle size was bigger than 50 nm, there was more than one crystal boundary on their surface, which could not be distinguished by XRD [43]. Similarly, another study with copper telluride nanostructures of different shapes showed that the relative intensities between the different XRD peaks depends on the particle shape [44].

7.2.6 Small angle X-ray scattering

X-ray scattering (XRS) techniques are used to characterize the crystal and particle size and the crystallographic phase, which all together determine the physical properties of the nanoparticle. Due to their small volume and limited coherence, XRS of nanoparticles is much weaker than that of bulk materials. The signal can be increased by either measuring the sample over a longer time or with high-flux sources (increased photons/sec). While high-flux sources provide superior signal-to-noise, they can have a detrimental effect on the sample due to radiation damage, which is particularly relevant for polymers or organic molecules such as surfactants that may be present as stabilizers on the nanoparticle surface [45].

Small angle X-ray scattering (SAXS) is widely used to determine the shape and size of materials in the range of 1 to 100 nm. SAXS is based on the elastic scattering of the electron cloud of each atom present in the sample and the difference in the electronic density of the scattering object and the medium. Typically, a SAXS sample is highly concentrated and can be a solid, powder, composite or a nanoparticle dispersion in liquid medium. Samples are then irradiated by a monochromatic X-ray beam and the X-ray detector records its scattering pattern, which can be expressed as a function of momentum transfer as $q = 4\pi \sin \theta/\lambda$, where λ is the wavelength of the incident beam and 2θ is the scattering angle. Being an ensemble method, SAXS probes a very large number of nanoparticles simultaneously and gives a statistically relevant average over a large proportion of the sample. Wang et al. compared SAXS and XRD to monitor the structural changes of platinum nanoparticles with temperature [46]. They observed that for some conditions, the sizes from XRD and SAXS did not correlate since SAXS is more sensitive to the size of the fluctuation region of electron density during thermal treatment.

7.2.7 Dynamic light scattering

Dynamic light scattering (DLS) is one of the most commonly used methods to analyse nanoparticle size. When particles are suspended in a liquid, they undergo constant random motion, known as Brownian motion, wherein each particle is constantly moving,

and its motion is not correlated with that of other particles. The diffusion of spherical particles can be described by the Stokes–Einstein equation:

$$D = \frac{\kappa_B T}{3\pi\eta\text{d}}$$

where, κ_B is the Boltzmann constant, T is the absolute temperature, η is the viscosity of the solvent, D is the diffusion coefficient of the particles, and d is the diameter of the particles. Accordingly, smaller particles move more rapidly in solution as compared to larger particles.

When a particle is irradiated by a visible light, a part of the light will be transmitted through the sample and a part can be absorbed by the sample (Figure 5A, B). For particles considerably smaller (at least 20-fold) than the wavelength (λ) of the incident radiation, the radiation will be scattered in different directions, without altering its wavelength or energy. This elastic scattering of light is known as Rayleigh scattering. As light scatters from the moving particles, the distance between particles varies with time which creates constructive and destructive interferences in the intensity of scattered light, resulting in time-dependent fluctuations in the intensity of the scattered light, which in DLS are measured by a fast photon counter. This fluctuation of scattered light intensity as a function of time reveals information on the velocity of the particles, known as the translation diffusion coefficient. As expected, larger particles will cause smaller fluctuation rates in the scattered light, whereas smaller, faster particles will result in higher fluctuation rates. From the translation diffusion coefficient, the hydrodynamic diameter of particles can be calculated using the Stokes-Einstein equation. The practical upper limit of the particle size determined using the DLS method is around 1–3 μm.

DLS is one of the most frequently used methods for size estimation of nanoparticles. Sample preparation and the measurement method for DLS are simple and straightforward. Since DLS depicts the intensity of scattered light as a function of particle size distribution, which can be converted to their contribution per volume or relative number, DLS can be used to observe subtle changes in particle sizes. For instance, diameter changes after silica coatings on gold nanoparticles have been described [47]. Due to the low contrast of silica, measurements by TEM correspond only to the metallic cores, whereas the results obtained by DLS correspond to the total size of the metallic core and the coating layer, enabling the assessment of the thickness of the coating layer. Another application is evaluating particle stability over different conditions. For example, Guidelli et al. determined the minimum concentration of a stabilizing agent required to prevent particle aggregation [48]. In 2013, Borissevitch et al. [49] used DLS to study the interaction and complex formation between CdSe/ZnS-PEGOH 570 Quantum Dots with negatively charged meso-tetrakis(p-sulfonato-phenyl)porphyrin (TPPS4). DLS has also been utilized to study the changes in particle diameters after encapsulation of small molecule drugs into polymeric micelles [50] or liposomes [51].

On the other hand, DLS measurements are also very sensitive to the salt concentration, pH or the buffer in which the nanoparticles are suspended. In a comprehensive study,

Huang et al. [52] demonstrated impact of polymer concentration, type of organic solvent, temperature, aqueous phase ionic strength, organic phase injection rate, aqueous phase agitation rate, gauge of the needles, and final polymer concentration on the size of the poly(D,L-lactic-co-glycolic acid) nanoparticles measured by DLS.

An important parameter for DLS measurements is the poly dispersity index (PDI). The intensity size distribution of particles is highly sensitive to small numbers of aggregates. If particle size distribution can be fitted to a Gaussian distribution, the PDI can be calculated as

$$PDI = \frac{\sigma}{R_h}$$

where, σ represents the standard deviation and R_h, the average hydrodynamic radius. A higher PDI indicates that the mixture contains particles of different sizes and the hydrodynamic diameter is the average of this mixture, irrespective of the relative contribution of each different particle (i.e. if 90% of the mixture has a diameter of 100 nm and only 10% has a diameter of 1000 nm, DLS measurements will result in an average diameter of 200-400 nm). In addition, size analyses of nonspherical particles by DLS must be performed with caution. Since the calculated diameter for DLS is calculated by the Stokes-Einstein equation, the diameter of a non-spherical particle will be approximated to that of a sphere diffusing in the same medium at the same velocity regardless of the particle shape. To circumvent this problem, Badaire et al. [53] used depolarized light for DLS measurements of the size of carbon nanotubes in suspension.

Taken together, considering that the limitations of DLS are mainly associated with particle geometry, it provides one of the most practical and fastest ways to study particle size distributions in monodispersed and polydispersed systems and the kinetics of size evolution under different conditions.

7.2.8 Tuneable resistive pulse sensing (TRPS)
Due to its ease of use, high throughput nature and broad applicability DLS is currently the preferred method for nanoparticle size characterization. However, when analyzing polydisperse systems, the Z-average value obtained after DLS measurements is not indicative of the neither population's actual hydrodynamic diameter. Recently, tuneable resistive pulse sensing (TRPS) has shown to be a highly sensitive method to determine individual particle sizes as well as the real size distribution, with similar accuracy to TEM, for a nanoparticle suspension. TRPS can be used for size estimations [54], with a lower detection limit of 40 nm, for concentration analysis, to analyse nanoparticle shape [55], [56], conductivity [57] and also surface charge [58], [59].

TRPS is based on the *Coulter principle,* wherein whenever a particle passes through a single pore in a thin membrane, separating cells filled with electrolytic solutions, the ionic current passing through that pore is blocked for a short period of time resulting in a "resistive pulse". This electric signal, proportional to the particle volume, is recorded and analysed for each particle, one after the other, thereby resulting in a particle-by-particle

size estimation, providing in the end number-weighted population statistics. TRPS uses a polyurethane membrane wherein the size of the nanopore can be 'tuned' [60] (Figure 5C-E). Since TRPS relies on changes in electric current, it requires conductive solutions for the analysis, making it incompatible to characterize nanoparticles under physiological buffer conditions.

Our group recently demonstrated that for siRNA-polymer polyplexes, which were largely monodisperse, particle sizes depending on used N/P ratios (ratio between excess polymer to siRNA) followed a similar trend [21]. Interestingly, DLS measurements performed in HEPES showed the smallest particle sizes and most efficient siRNA packaging at a polymer per siRNA excess of N/P 5.5. On the other hand, in the high ionic strength TRPS electrolyte solutions, the smallest particles were observed at N/P 4. Although the TRPS data displayed slightly higher mean diameters, the average sizes as well as the number-weighted distribution profiles were in acceptable agreement with DLS data.

Pal and colleagues directly compared TRPS and DLS to characterize polydisperse dispersions of engineered nanomaterials in complex cell culture medium, containing serum, mimicking *in vitro* testing conditions [61]. They performed serial dilutions of the engineered nanomaterial dispersions over the 0.5–50 µg/mL concentration range in RPMI+10% FBS. In nanotoxicology studies, lower nanoparticle concentrations have shown to be better tolerated (<1 mg/ml), thus the characterization of nanomaterials at low doses is critical. Their results, summarized in Figure 6 and Table 1, show that DLS produced very broad unimodal size distributions across all concentrations. The measured average hydrodynamic diameter decreased from 311 nm (at 50 µg/mL) to 43 nm (at 0.5 µg/mL), this later peak corresponding to serum proteins (confirmed with blanks). In addition, the PDI increased from 0.3 to 0.4 to 1 below 1 µg/mL. On the other hand, TRPS size distributions were bimodal (peaks at 220 and 660 nm), which did not change notably as a function of their concentration. In addition, since TRPS has a lower cut-point at 40 nm, serum proteins were not measured. As expected, the frequency at which the particles went through the pore also dropped from 1000 particles/min (at 50 µg/ml) to 134 particles/min (at 0.5µg/ml).

Further, TRPS also provides indirect information on particle shape. For particles of similar dimensions, for instance, it was shown that the resistive pulse signal of a rod is significantly different from that of a sphere [56]. The resistive pulse of a particle with different shapes can be distinguished by the blockage event magnitude, revealing particle size and the full width at half maximum duration, related to the time taken for the particle to traverse the pore, dependent on its speed and length.

7.2.9 Nanoparticle tracking analysis
One of the more recent techniques, nanoparticle tracking analysis (NTA), is an innovation system to characterize the size of nanoparticles. In NTA, the particles, moving under Brownian motion, are illuminated by a laser beam and the light scattered by them is recorded by a microscope camera (Figure 7). Thus, each individual particle can be tracked and its hydrodynamic diameter can be calculated based on a modified Stokes-Einstein equation. For NTA, the measurable size range is between about 50 - 1,000 nm,

depending on the refractive index of the analysed particles. With real time monitoring, subtle changes in the characteristics of particle populations, such as aggregation or disassembly under different conditions (eg. thermal stress) can be observed and confirmed by visual validation. In addition, NTA can also provide approximate particle concentrations. Filipe et al [62] compared NTA and DLS measurements of polystyrene particles and protein aggregates. Both techniques showed good sizing accuracy and narrow distributions for all monodisperse samples (polystyrene beads). However, when beads of two different sizes were mixed together to result in a polydisperse system, NTA was able to resolve and distinguish the two size populations in all mixtures, resulting in accurate size estimations of the beads in the mixtures (Figure 8). On the other hand, DLS resulted in a broad single peak, shifted towards the larger sizes present.

7.3 Surface Charge

Surface chemistry and charge play critical roles in nanoparticle stability and aggregation, cellular uptake [63], [64], [65], [66], *in vivo* biodistribution [67], cytotoxicity, activation of the immune system [68] and the development and composition of the protein 'corona' that develops around the nanoparticles *in vivo* [69].

Generally, positively charged nanoparticles have been shown to be taken up more efficiently via phagocytosis than neutral or negatively charged particles, irrespective of their composition [66]. On the other hand, slightly negatively charged nanoparticles were shown to be taken up by tumour cells more efficiently with low liver uptake [64]. In addition, negatively charged samples also did not significantly adsorb proteins thereby reducing their clearance by the reticuloendothelial system (RES) and improving *in vivo* compatibility. By varying the surface charges, one can thus vary the electrostatic interaction between the nanoparticles and serum proteins thereby affecting the fate of nanoparticles administered in biological systems.

The surface charge of nanocarriers can be inferred to by measuring their **Zeta potential** (**ζ-potential**), which describes the electrokinetic potential in colloidal dispersion. The ζ-potential represents the electrostatic potential at the plane of shear and typically samples with ζ-potential values higher (or equal to) $\pm 20 - 30$ mV form stable colloidal suspensions that do not tend to agglomerate [70]. Current characterisation methodologies are based on ensemble measurements (e.g. phase analysis light scattering, laser doppler anemometry, streaming potentiometry) that measure the average electrophoretic mobility of particles in suspension. However, while dealing with polydisperse systems (such as polyelectrolyte complexes) that contain a heterogeneous mixture of a range of ζ-potentials, an ensemble approach is problematic. Using resistive pulse sensing, Deblois et al. [71] first performed single particle electrokinetic measurements, which are discussed at the end.

7.3.1 Laser doppler anemometry

One method for the measurement of the ζ-potential is based on the relative electrophoretic motion of particles and electrolytes within an applied electric field. In this technique, voltage is applied across a pair of electrodes at the ends of a cell containing the particle suspension and is irradiated with laser light. The particles are attracted to the

oppositely charged electrode, and the velocity of the particles can be measure by observing the Doppler shift in the scattered light. The direction and velocity of motion of the nanoparticles is a function of their charge, the suspension medium and the strength of the applied electric field. Their mobility can then be calculated as the ratio of the velocity to the applied electric field strength.

$$U = \frac{\lambda.\, Vd}{2E.\, n.\, Sin\left(\frac{\theta}{2}\right)}$$

where, λ is the wavelength of the laser light; *Vd*, the particle velocity determined by the Doppler shift; E, the applied electric field strength; n, the refractive index of the solvent used and the scattered light angle, θ.

Subsequently, the ζ-potential can be calculated according to the electric potential of the particle at the shear plane using the following relationship

$$\zeta = \frac{U\eta}{\varepsilon f(ka)}$$

where, U is the electrical mobility; ε, the dielectric constant of the solvent; η, the solvent viscosity and f(ka), the Henry coefficient.

Interstingly, Liao and colleagues demonstrated the pH dependence of ζ-potential of Titanium oxide (TiO_2) particles irrespective of their size and shape [44]. Similarly, Sharma et al. observed pH-dependency of the ζ-potential of magnetic iron oxide nanoparticles coated with citrate, PEG-PEI, CM-dextran, dextran, and methoxy-PEG-phosphate + rutin over a pH range from 2 to 10 [47]. They observed that the citrate or PEG-PEI coated precursor magnetic iron oxide particles had a strongly positive ζ-potential at pH <3, i.e. around 40 mV while other polymers displayed a mildly positive ζ-potential (< 10 mV) at low pH values (Figure 9). Interestingly, all polymer coatings except PEG-PEI demonstrated negative ζ-potentials at higher pH (pH > 5) while PEG-PEI had a positive ζ-potential across the entire pH range tested. The advantages of laser Doppler anemometry are that the method requires minimal sample preparation, can analyse multiple samples, provides results with good statistics, and, by using disposable cuvettes, avoids cross contamination between samples.

7.3.2 Single particle electro-kinetic measurements

TRPS can be used to measure the surface charge of particles in suspension, enabling single particle surface-charge measurements leading to robust and reproducible ζ-potential measurements. This property is based on the resistive signal duration as a function of the applied pressure or voltage across the pore. The average electrophoretic mobility shift is then calculated with respect to the calibration standards (carboxylated polystyrene particles, for example) with known average ζ-potentials. The step by step calibration process and the consecutive zeta potential calculation of the sample on a particle-by-particle basis have been explained in detail by Blundell *et al* [72] and Vogel

et al. [73, 74]. Briefly, there is a linear relationship of electrokinetic (electroosmotic and electrophoretic) particle velocities of sample and calibration and their respective ζ-potentials, based on the Smoluchowski approximation [75].

7.4 Porosity

Over the last decade, mesoporous nanoparticles have been actively investigated in the areas of drug delivery and imaging. Mesoporous nanoparticles can be made of inorganic materials, often silicon or silica. The most remarkable advantage of mesoporous nanoparticles as drug carriers is their extremely high surface to volume ratio, large surface area ($700 - 1000$ m^2/g), and large pore volume (> 0.9 cm3/g) [76], [77] while still maintaining a thermally, mechanically and chemically stable and rigid framework [78]. The small size of the pores confines the space of a drug and engages the effects of surface interactions of the drug molecules and the pore wall. Pore diameters of mesoporous materials lie between $2–50$ nm, allowing high payloads of therapeutic molecules while protecting them from premature release and degradation [76]. Thus, they can be used to deliver large doses of hydrophobic drugs to target organs, at a controllable release rate [79].

Porosimetry is a useful technique for the characterization of porous materials, providing information about the pore size, pore volume, and surface area of a sample [80]. The technique is based on the intrusion of a non-wetting liquid (such as Mercury) into the voids in a porous sample. As pressure is applied, mercury fills the larger pores and further proceeds to fill the smaller pores as the applied pressure increases. Using mercury porosimetry, pores between about 250 µm and 3.5 nm can be investigated [80]. Using the Washburn Equation the pore diameter (D_P) can be calculated as

$$D_P = -\frac{4\sigma cos\theta}{(P_L - P_G)}$$

where, σ is the surface tension of mercury; θ, the contact angle of mercury (between $135°$ -$142°$ for most solids), P_L the pressure applied to mercury and P_G, the gas pressure (since the assay is usually performed in a vacuum, this value is 0) [80].

7.5 Viscosity

The viscosity of a nanoparticle suspension significantly influences its injectability, since high viscosities require high injection forces. In addition, highly viscous fluids should not be injected intravenously due to the risk of pulmonary embolism [81] and should be administered subcutaneously. Interestingly, a very low viscosity of a subcutaneously injected solution has also been associated with an increased sensation of pain. Berteau and colleagues compared the pain perceived after subcutaneous injections of three different fluid viscosities (1, 8–10, and 15–20 cP) and observed that high viscosity injections (up to 15–20 cP) were less painful and, consequently, the most easily tolerated ones [82]. Since the application route of nanoparticle suspensions depends on their viscosity, knowledge of their rheological properties becomes crucial. Particle size, shape, concentration and temperature affect the nanosuspension viscosity [83], and Rudyak and colleagues reported that nanoparticle size had the strongest impact on viscosity as measured by rheology [84].

Rheology studies flow behavior and is normally applied to fluid or 'soft solid' materials, such as hydrogels. Flow is typically measured using shear stress and its parameters, stress (τ) and strain rate (γ) are calculated from measurements of torque and flow rate. Viscosity (η) is defined as

$$\eta = \frac{\tau}{\gamma}$$

Experimentally, a rheometer can measure the viscoelasticity, yield stress, thixotropy, extensional viscosity and stress relaxation behavior of the suspension. There are three main types of rheometers: capillary, torque, and dynamic rotational. For a capillary rheometer, the sample is forced to flow through a capillary of well-defined dimensions under high pressure, and the pressure drop across the capillary is measured resulting in pressure-flow rate data for the fluid, from which viscosity is calculated. Temperature and shear rate can be closely controlled to simulate the processing environment of interest and smaller sample volumes can be evaluated, which may be beneficial for more expensive formulations, such as nucleic acids or monoclonal antibodies [85]. A torque rheometer resembles an extruder and measures the torque on the mixing screws or rotors, which reflects how hard it is to mix the material and can be correlated to viscosity [86]. While both capillary and torque rheometers typically provide data on viscosity and melt flow as material passes through the instrument, dynamic rotational or oscillatory rheometers probe into a polymer's molecular structure and viscoelastic properties. These instruments place the plastic sample between two components, one stationary and one that turns back and forth at adjustable speed and operate at relatively low shear stress.

An ideal fluid flows in Newtonian behavior, with a linear relationship between stress and strain rate and zero stress at zero strain rate. However, only a small number of fluids exhibit such constant viscosity. Most fluids show non-Newtonian behavior, of which most commonly demonstrate plastic or pseudoplastic behaviours. For plastic fluids flow only initiates after a certain level of stress is applied (yield stress), however, once attained, subsequently the relationship between stress and strain rate is linear. On the other hand, for pseudoplastic fluids viscosity decreases as strain rate increases [87].

7.6 Concluding remarks and future perspectives
Nanomaterials have great potential for use in drug delivery, improving drug stability and release *in vivo* while minimizing toxic side effects. Over the last decade, a rapid growth in the development of nanocarrier systems has been described, which exist in various chemical compositions ranging from micelles to metals or metal oxides, synthetic polymers or biomolecules. Each of these materials features a completely different chemistry, surface properties and interaction potential, particularly with proteins *in vivo*. The choice of the nanoparticle characterization techniques depends at first, on their physical form, i.e. solid samples and powders or suspensions. Solid or dry samples provide considerable freedom in the choice of technique and can be analysed by electron microscopy, AFM or X-ray scattering. Nanoparticle suspensions, on the other hand are more challenging, especially in case of high polydispersity, and can be evaluated by light scattering or NTA techniques. Characterization of the surface charge is almost always

performed by electrophoretic methods, irrespective of particle state. Subsequently, it is imperative to characterise nanoparticles under the envisioned biological operating conditions of the nanomaterial. Components of biological fluids, such as proteins, often interact with and assemble with the nanoparticles, resulting in the formation of a protein corona, thereby altering their initial surface properties (Box 1). In summary, to get a full picture of the physico-chemical characteristics of nanoparticles, typically a combination of the techniques described here is essential. In fact, even to analyse a single parameter, such as size, a combination of techniques may need to be employed.

Acknowledgements

Important notes

- Nanoparticle characterization is a major obstacle in nanoscience and is unfortunately cannot be addressed in a straightforward manner.
- Nanoparticles possess unique physicochemical properties due to their high surface area and nanoscale size, depending on their shape, size and structure.
- Different physicochemical properties define the structure-function relationship (*in vivo*) of a nanoparticle and precise evaluation of each (especially shape, size, charge and porosity) is critical.
- Measuring these properties is important for translating the potential benefits of nanoparticles into specific applications in drug delivery or as diagnostic tools.

Questions for future research

- **How does one decide what is the best method to use?** In most conditions, a combination of methods is required to fully characterize a sample. The choice of methods depends on prior the nanoparticles' physical form, whether dry, poweders or colloidal suspensions. In addition, if the nanocarriers are sensitive to high energy electron beams or whether they have crystalline structures. Polydispersity of the samples also adds an additional parameter to consider, especially when light scattering methods are used. Moreover, nanoparticles should be characterized in buffers that mimic the pH, temperature and ionic strength that the nanoparticles would encounter *in vivo* as closely as possible.
- **Does the nanoparticle result in the formation of a protein corona in contact with plasma?** This depends on the particle size, surface topology and composition. The formation of a protein corona around the nanoparticles result in decreased activity by masking the surface of the particles as well as resulting in immune recognition. Therefore, depending on the presence or absence of a protein corona,

the same NPs can induce different biological outcomes.

References

[1] B. European Commission, Belgium, Commission Recommendation of 18 October 2011 on the definition of nanomaterial, 2011. https://ec.europa.eu/environment/chemicals/nanotech/faq/definition_en.htm.

[2] D.S. Kohane, Microparticles and nanoparticles for drug delivery, Biotechnology and bioengineering 96(2) (2007) 203-9.

[3] K. Cho, X. Wang, S. Nie, Z.G. Chen, D.M. Shin, Therapeutic nanoparticles for drug delivery in cancer, Clinical cancer research : an official journal of the American Association for Cancer Research 14(5) (2008) 1310-6.

[4] E. Allard, C. Passirani, J.P. Benoit, Convection-enhanced delivery of nanocarriers for the treatment of brain tumors, Biomaterials 30(12) (2009) 2302-18.

[5] Y. Xie, N.H. Kim, V. Nadithe, D. Schalk, A. Thakur, A. Kilic, L.G. Lum, D.J.P. Bassett, O.M. Merkel, Targeted delivery of siRNA to activated T cells via transferrin-polyethylenimine (Tf-PEI) as a potential therapy of asthma, Journal of controlled release : official journal of the Controlled Release Society 229 (2016) 120-129.

[6] D. Peer, J.M. Karp, S. Hong, O.C. Farokhzad, R. Margalit, R. Langer, Nanocarriers as an emerging platform for cancer therapy, Nature nanotechnology 2(12) (2007) 751-60.

[7] T.M. Allen, Ligand-targeted therapeutics in anticancer therapy, Nature reviews. Cancer 2(10) (2002) 750-63.

[8] S. Hirn, M. Semmler-Behnke, C. Schleh, A. Wenk, J. Lipka, M. Schäffler, S. Takenaka, W. Möller, G. Schmid, U. Simon, Particle size-dependent and surface charge-dependent biodistribution of gold nanoparticles after intravenous administration, European journal of pharmaceutics and biopharmaceutics 77(3) (2011) 407-416.

[9] X. Huang, L. Li, T. Liu, N. Hao, H. Liu, D. Chen, F. Tang, The shape effect of mesoporous silica nanoparticles on biodistribution, clearance, and biocompatibility in vivo, ACS nano 5(7) (2011) 5390-5399.

[10] Q. Mu, G. Jiang, L. Chen, H. Zhou, D. Fourches, A. Tropsha, B. Yan, Chemical basis of interactions between engineered nanoparticles and biological systems, Chem Rev 114(15) (2014) 7740-81.

[11] L. Guo, A. Von Dem Bussche, M. Buechner, A. Yan, A.B. Kane, R.H. Hurt, Adsorption of essential micronutrients by carbon nanotubes and the implications for nanotoxicity testing, Small 4(6) (2008) 721-7.

[12] M.P. Desai, V. Labhasetwar, E. Walter, R.J. Levy, G.L. Amidon, The mechanism of uptake of biodegradable microparticles in Caco-2 cells is size dependent, Pharmaceutical research 14(11) (1997) 1568-73.

[13] M. Gaumet, A. Vargas, R. Gurny, F. Delie, Nanoparticles for drug delivery: the need for precision in reporting particle size parameters, European journal of pharmaceutics and biopharmaceutics : official journal of Arbeitsgemeinschaft fur Pharmazeutische Verfahrenstechnik e.V 69(1) (2008) 1-9.

[14] F. Alexis, E. Pridgen, L.K. Molnar, O.C. Farokhzad, Factors Affecting the Clearance and Biodistribution of Polymeric Nanoparticles, Molecular Pharmaceutics 5(4) (2008) 505-515.

[15] A.S. Hoffman, The origins and evolution of "controlled" drug delivery systems, Journal of controlled release : official journal of the Controlled Release Society 132(3) (2008) 153-63.

[16] A. Prokop, J.M. Davidson, Nanovehicular intracellular delivery systems, Journal of pharmaceutical sciences 97(9) (2008) 3518-90.

[17] X. Xiong, Y. Wang, W. Zou, J. Duan, Y. Chen, Preparation and Characterization of Magnetic Chitosan Microcapsules, Journal of Chemistry 2013 (2013) 8.

[18] D.B. Williams, C.B. Carter, P. Veyssiere, Transmission electron microscopy: a textbook for materials science, MRS Bulletin-Materials Research Society 23(5) (1998) 47.

[19] He, Ge, Liu, Wang, Zhang, Synthesis of Cagelike Polymer Microspheres with Hollow Core/Porous Shell Structures by Self-Assembly of Latex Particles at the Emulsion Droplet Interface, Chemistry of Materials 17(24) (2005) 5891-5892.

[20] A. Bogner, P.H. Jouneau, G. Thollet, D. Basset, C. Gauthier, A history of scanning electron microscopy developments: towards "wet-STEM" imaging, Micron 38(4) (2007) 390-401.

[21] N. Hartl, F. Adams, G. Costabile, L. Isert, M. Doblinger, X. Xiao, R. Liu, O.M. Merkel, The Impact of Nylon-3 Copolymer Composition on the Efficiency of siRNA Delivery to Glioblastoma Cells, Nanomaterials 9(7) (2019).

[22] M. Adrian, J. Dubochet, J. Lepault, A.W. McDowall, Cryo-electron microscopy of viruses, Nature 308(5954) (1984) 32-6.

[23] N.M. Belliveau, J. Huft, P.J. Lin, S. Chen, A.K. Leung, T.J. Leaver, A.W. Wild, J.B. Lee, R.J. Taylor, Y.K. Tam, C.L. Hansen, P.R. Cullis, Microfluidic Synthesis of Highly Potent Limit-size Lipid Nanoparticles for In Vivo Delivery of siRNA, Molecular therapy. Nucleic acids 1 (2012) e37.

[24] C. Bonnaud, C.A. Monnier, D. Demurtas, C. Jud, D. Vanhecke, X. Montet, R. Hovius, M. Lattuada, B. Rothen-Rutishauser, A. Petri-Fink, Insertion of nanoparticle clusters into vesicle bilayers, ACS Nano 8(4) (2014) 3451-60.

[25] U. Baxa, Imaging of Liposomes by Transmission Electron Microscopy, Methods in molecular biology 1682 (2018) 73-88.

[26] P.P. Wibroe, D. Ahmadvand, M.A. Oghabian, A. Yaghmur, S.M. Moghimi, An integrated assessment of morphology, size, and complement activation of the PEGylated liposomal doxorubicin products Doxil(R), Caelyx(R), DOXOrubicin, and SinaDoxosome, Journal of controlled release : official journal of the Controlled Release Society 221 (2016) 1-8.

[27] T.S. Baker, N.H. Olson, S.D. Fuller, Adding the third dimension to virus life cycles: three-dimensional reconstruction of icosahedral viruses from cryo-electron micrographs, Microbiology and molecular biology reviews : MMBR 63(4) (1999) 862-922, table of contents.

[28] S. Kler, J.C. Wang, M. Dhason, A. Oppenheim, A. Zlotnick, Scaffold properties are a key determinant of the size and shape of self-assembled virus-derived particles, ACS chemical biology 8(12) (2013) 2753-61.

[29] Y. Tian, T. Wang, W. Liu, H.L. Xin, H. Li, Y. Ke, W.M. Shih, O. Gang, Prescribed nanoparticle cluster architectures and low-dimensional arrays built using octahedral DNA origami frames, Nature nanotechnology 10(7) (2015) 637-44.

[30] T.I. Lobling, J.S. Haataja, C.V. Synatschke, F.H. Schacher, M. Muller, A. Hanisch, A.H. Groschel, A.H. Muller, Hidden structural features of multicompartment micelles revealed by cryogenic transmission electron tomography, ACS Nano 8(11) (2014) 11330-40.

[31] G. Binnig, C.F. Quate, C. Gerber, Atomic Force Microscope, Physical Review Letters 56(9) (1986) 930-933.

[32] H.J. Kim, S.K. Choi, S.H. Kang, K.H. Oh, Structural phase transitions of Ge2Sb2Te5 cells with TiN electrodes using a homemade W heater tip, Applied Physics Letters 90(8) (2007) 083103.

[33] D.R. Lovley, N.S. Malvankar, Seeing is believing: novel imaging techniques help clarify microbial nanowire structure and function, Environmental microbiology 17(7) (2015) 2209-15.

[34] P. Xiao, J. Gu, J. Chen, J. Zhang, R. Xing, Y. Han, J. Fu, W. Wang, T. Chen, Micro-contact printing of graphene oxide nanosheets for fabricating patterned polymer brushes, Chemical communications 50(54) (2014) 7103-6.

[35] N. Gadegaard, Atomic force microscopy in biology: technology and techniques, Biotechnic & Histochemistry 81(2-3) (2006) 87-97.

[36] A. Stylianou, S.V. Kontomaris, C. Grant, E. Alexandratou, Atomic Force Microscopy on Biological Materials Related to Pathological Conditions, Scanning 2019 (2019) 8452851.

[37] F.M. Etzler, J. Drelich, Chapter 6 - Atomic Force Microscopy for Characterization of Surfaces, Particles, and Their Interactions, in: R. Kohli, K.L. Mittal (Eds.), Developments in Surface Contamination and Cleaning, William Andrew Publishing, Oxford, 2012, pp. 307-331.

[38] H. Zhou, Q. Xu, S. Li, Y. Zheng, X. Wu, C. Gu, Y. Chen, J. Zhong, Dynamic enhancement in adhesion forces of truncated and nanosphere tips on substrates, RSC Advances 5(111) (2015) 91633-91639.

[39] J. Zhong, W. Zheng, L. Huang, Y. Hong, L. Wang, Y. Qiu, Y. Sha, PrP106-126 amide causes the semi-penetrated poration in the supported lipid bilayers, Biochimica et biophysica acta 1768(6) (2007) 1420-9.

[40] N. Shamitko-Klingensmith, J. Legleiter, Investigation of temperature induced mechanical changes in supported bilayers by variants of tapping mode atomic force microscopy, Scanning 37(1) (2015) 23-35.

[41] J.H. Hafner, C.L. Cheung, A.T. Woolley, C.M. Lieber, Structural and functional imaging with carbon nanotube AFM probes, Progress in biophysics and molecular biology 77(1) (2001) 73-110.

[42] S.K. Jones, A. Sarkar, D.P. Feldmann, P. Hoffmann, O.M. Merkel, Revisiting the value of competition assays in folate receptor-mediated drug delivery, Biomaterials 138 (2017) 35-45.

[43] S. Upadhyay, K. Parekh, B. Pandey, Influence of crystallite size on the magnetic properties of Fe3O4 nanoparticles, Journal of Alloys and Compounds 678 (2016) 478-485.

[44] M.-H. Liao, C.-H. Hsu, D.-H. Chen, Preparation and properties of amorphous titania-coated zinc oxide nanoparticles, Journal of Solid State Chemistry 179(7) (2006) 2020-2026.

[45] B. Ingham, X-ray scattering characterisation of nanoparticles, Crystallography Reviews 21(4) (2015) 229-303.

[46] W. Wang, X. Chen, Q. Cai, G. Mo, L.S. Jiang, K. Zhang, Z.J. Chen, Z.H. Wu, W. Pan, In situ SAXS study on size changes of platinum nanoparticles with temperature, Eur. Phys. J. B 65(1) (2008) 57-64.

[47] A. Sharma, C. Cornejo, J. Mihalic, A. Geyh, D.E. Bordelon, P. Korangath, F. Westphal, C. Gruettner, R. Ivkov, Physical characterization and in vivo organ distribution of coated iron oxide nanoparticles, Scientific Reports 8(1) (2018) 4916.

[48] E.J. Guidelli, A.P. Ramos, M.E. Zaniquelli, P. Nicolucci, O. Baffa, Synthesis and characterization of silver/alanine nanocomposites for radiation detection in medical applications: the influence of particle size on the detection properties, Nanoscale 4(9) (2012) 2884-93.

[49] I.E. Borissevitch, G.G. Parra, V.E. Zagidullin, E.P. Lukashev, P.P. Knox, V.Z. Paschenko, A.B. Rubin, Cooperative effects in CdSe/ZnS-PEGOH quantum dot luminescence quenching by a water soluble porphyrin, Journal of Luminescence 134 (2013) 83-87.

[50] M. Yokoyama, A. Satoh, Y. Sakurai, T. Okano, Y. Matsumura, T. Kakizoe, K. Kataoka, Incorporation of water-insoluble anticancer drug into polymeric micelles and control of their particle size, Journal of Controlled Release 55(2) (1998) 219-229.

[51] M. Zaru, C. Sinico, A. De Logu, C. Caddeo, F. Lai, M.L. Manca, A.M. Fadda, Rifampicin-loaded liposomes for the passive targeting to alveolar macrophages: in vitro and in vivo evaluation, Journal of Liposome Research 19(1) (2009) 68-76.

[52] W. Huang, C. Zhang, Tuning the Size of Poly(lactic-co-glycolic Acid) (PLGA) Nanoparticles Fabricated by Nanoprecipitation, Biotechnology journal 13(1) (2018).

[53] S. Badaire, P. Poulin, M. Maugey, C. Zakri, In situ measurements of nanotube dimensions in suspensions by depolarized dynamic light scattering, Langmuir 20(24) (2004) 10367-10370.

[54] D. Kozak, W. Anderson, R. Vogel, S. Chen, F. Antaw, M. Trau, Simultaneous size and zeta-potential measurements of individual nanoparticles in dispersion using size-tunable pore sensors, ACS Nano 6(8) (2012) 6990-7.

[55] D.C. Golibersuch, Observation of aspherical particle rotation in Poiseuille flow via the resistance pulse technique. I. Application to human erythrocytes, Biophysical journal 13(3) (1973) 265-80.

[56] M. Platt, G.R. Willmott, G.U. Lee, Resistive pulse sensing of analyte-induced multicomponent rod aggregation using tunable pores, Small 8(15) (2012) 2436-44.

[57] D.A. Holden, G. Hendrickson, L.A. Lyon, H.S. White, Resistive Pulse Analysis of Microgel Deformation During Nanopore Translocation, The journal of physical chemistry. C, Nanomaterials and interfaces 115(7) (2011) 2999-3004.

[58] T. Ito, L. Sun, M.A. Bevan, R.M. Crooks, Comparison of nanoparticle size and electrophoretic mobility measurements using a carbon-nanotube-based coulter counter, dynamic light scattering, transmission electron microscopy, and phase analysis light scattering, Langmuir 20(16) (2004) 6940-5.

[59] T. Ito, L. Sun, R.M. Crooks, Simultaneous determination of the size and surface charge of individual nanoparticles using a carbon nanotube-based Coulter counter, Analytical chemistry 75(10) (2003) 2399-406.

[60] S.J. Sowerby, M.F. Broom, G.B. Petersen, Dynamically resizable nanometre-scale apertures for molecular sensing, Sensors and Actuators B: Chemical 123(1) (2007) 325-330.

[61] A.K. Pal, I. Aalaei, S. Gadde, P. Gaines, D. Schmidt, P. Demokritou, D. Bello, High resolution characterization of engineered nanomaterial dispersions in complex media using tunable resistive pulse sensing technology, ACS Nano 8(9) (2014) 9003-15.

[62] V. Filipe, A. Hawe, W. Jiskoot, Critical evaluation of Nanoparticle Tracking Analysis (NTA) by NanoSight for the measurement of nanoparticles and protein aggregates, Pharmaceutical research 27(5) (2010) 796-810.

[63] E.C. Cho, J. Xie, P.A. Wurm, Y. Xia, Understanding the Role of Surface Charges in Cellular Adsorption versus Internalization by Selectively Removing Gold Nanoparticles on the Cell Surface with a I2/KI Etchant, Nano Letters 9(3) (2009) 1080-1084.

[64] K. Xiao, Y. Li, J. Luo, J.S. Lee, W. Xiao, A.M. Gonik, R.G. Agarwal, K.S. Lam, The effect of surface charge on in vivo biodistribution of PEG-oligocholic acid based micellar nanoparticles, Biomaterials 32(13) (2011) 3435-46.

[65] K. Saha, S.T. Kim, B. Yan, O.R. Miranda, F.S. Alfonso, D. Shlosman, V.M. Rotello, Surface functionality of nanoparticles determines cellular uptake mechanisms in mammalian cells, Small 9(2) (2013) 300-305.

[66] D.H. Jo, J.H. Kim, T.G. Lee, J.H. Kim, Size, surface charge, and shape determine therapeutic effects of nanoparticles on brain and retinal diseases, Nanomedicine: Nanotechnology, Biology and Medicine 11(7) (2015) 1603-1611.

[67] S.G. Elci, Y. Jiang, B. Yan, S.T. Kim, K. Saha, D.F. Moyano, G. Yesilbag Tonga, L.C. Jackson, V.M. Rotello, R.W. Vachet, Surface Charge Controls the Suborgan Biodistributions of Gold Nanoparticles, ACS Nano 10(5) (2016) 5536-5542.

[68] D.F. Moyano, M. Goldsmith, D.J. Solfiell, D. Landesman-Milo, O.R. Miranda, D. Peer, V.M. Rotello, Nanoparticle Hydrophobicity Dictates Immune Response, Journal of the American Chemical Society 134(9) (2012) 3965-3967.

[69] C.C. Fleischer, C.K. Payne, Nanoparticle–Cell Interactions: Molecular Structure of the Protein Corona and Cellular Outcomes, Accounts of Chemical Research 47(8) (2014) 2651-2659.

[70] S. Mourdikoudis, R.M. Pallares, N.T.K. Thanh, Characterization techniques for nanoparticles: comparison and complementarity upon studying nanoparticle properties, Nanoscale 10(27) (2018) 12871-12934.

[71] R.W. DeBlois, C.P. Bean, R.K. Wesley, Electrokinetic measurements with submicron particles and pores by the resistive pulse technique, Journal of colloid and interface science 61(2) (1977) 323-335.

[72] E.L. Blundell, R. Vogel, M. Platt, Particle-by-Particle Charge Analysis of DNA-Modified Nanoparticles Using Tunable Resistive Pulse Sensing, Langmuir 32(4) (2016) 1082-90.

[73] R. Vogel, F.A. Coumans, R.G. Maltesen, A.N. Boing, K.E. Bonnington, M.L. Broekman, M.F. Broom, E.I. Buzas, G. Christiansen, N. Hajji, S.R. Kristensen, M.J. Kuehn, S.M. Lund, S.L. Maas, R. Nieuwland, X. Osteikoetxea, R. Schnoor, B.J. Scicluna, M. Shambrook, J. de Vrij, S.I. Mann, A.F. Hill, S. Pedersen, A standardized method to determine the concentration of extracellular vesicles using tunable resistive pulse sensing, Journal of extracellular vesicles 5 (2016) 31242.

[74] R. Vogel, A.K. Pal, S. Jambhrunkar, P. Patel, S.S. Thakur, E. Reátegui, H.S. Parekh, P. Saá, A. Stassinopoulos, M.F. Broom, High-Resolution Single Particle Zeta Potential Characterisation of Biological Nanoparticles using Tunable Resistive Pulse Sensing, Scientific Reports 7(1) (2017) 17479.

[75] A. Sikora, D. Bartczak, D. Geißler, V. Kestens, G. Roebben, Y. Ramaye, Z. Varga, M. Palmai, A.G. Shard, H. Goenaga-Infante, C. Minelli, A systematic comparison of different techniques to determine the zeta potential of silica nanoparticles in biological medium, Analytical Methods 7(23) (2015) 9835-9843.

[76] J. Salonen, A.M. Kaukonen, J. Hirvonen, V.P. Lehto, Mesoporous silicon in drug delivery applications, Journal of pharmaceutical sciences 97(2) (2008) 632-53.

[77] M. Vallet-Regi, Nanostructured mesoporous silica matrices in nanomedicine, Journal of internal medicine 267(1) (2010) 22-43.

[78] H.A. Santos, L.M. Bimbo, V.P. Lehto, A.J. Airaksinen, J. Salonen, J. Hirvonen, Multifunctional porous silicon for therapeutic drug delivery and imaging, Current drug discovery technologies 8(3) (2011) 228-49.

[79] S.P. Hudson, R.F. Padera, R. Langer, D.S. Kohane, The biocompatibility of mesoporous silicates, Biomaterials 29(30) (2008) 4045-55.

[80] H. Giesche, Mercury Porosimetry: A General (Practical) Overview, Particle & Particle Systems Characterization 23(1) (2006) 9-19.

[81] D.M. Weir, L.A. Herzenberg, C. Blackwell, L.A. Herzenberg, Handbook of experimental immunology, Blackwell Scientific Publications, Oxford; Boston, 1986.

[82] C. Berteau, O. Filipe-Santos, T. Wang, H.E. Rojas, C. Granger, F. Schwarzenbach, Evaluation of the impact of viscosity, injection volume, and injection flow rate on subcutaneous injection tolerance, Medical devices 8 (2015) 473-84.

[83] I.M. Mahbubul, R. Saidur, M.A. Amalina, Latest developments on the viscosity of nanofluids, International Journal of Heat and Mass Transfer 55(4) (2012) 874-885.

[84] V.Y. Rudyak, S.L. Krasnolutskii, Dependence of the viscosity of nanofluids on nanoparticle size and material, Physics Letters A 378(26) (2014) 1845-1849.

[85] S.D. Hudson, P. Sarangapani, J.A. Pathak, K.B. Migler, A microliter capillary rheometer for characterization of protein solutions, Journal of pharmaceutical sciences 104(2) (2015) 678-85.

[86] A.O. Ogah, J.N. Afiukwa, A.A. Nduji, Characterization and Comparison of Rheological Properties of Agro Fiber Filled High-Density Polyethylene Bio-Composites, Open Journal of Polymer Chemistry Vol.04No.01 (2014) 8.

[87] H.A. Barnes, J.F. Hutton, K. Walters, An introduction to rheology, Elsevier : Distributors for the U.S. and Canada, Elsevier Science Pub. Co., Amsterdam ; New York, 1989.

Figures and Tables
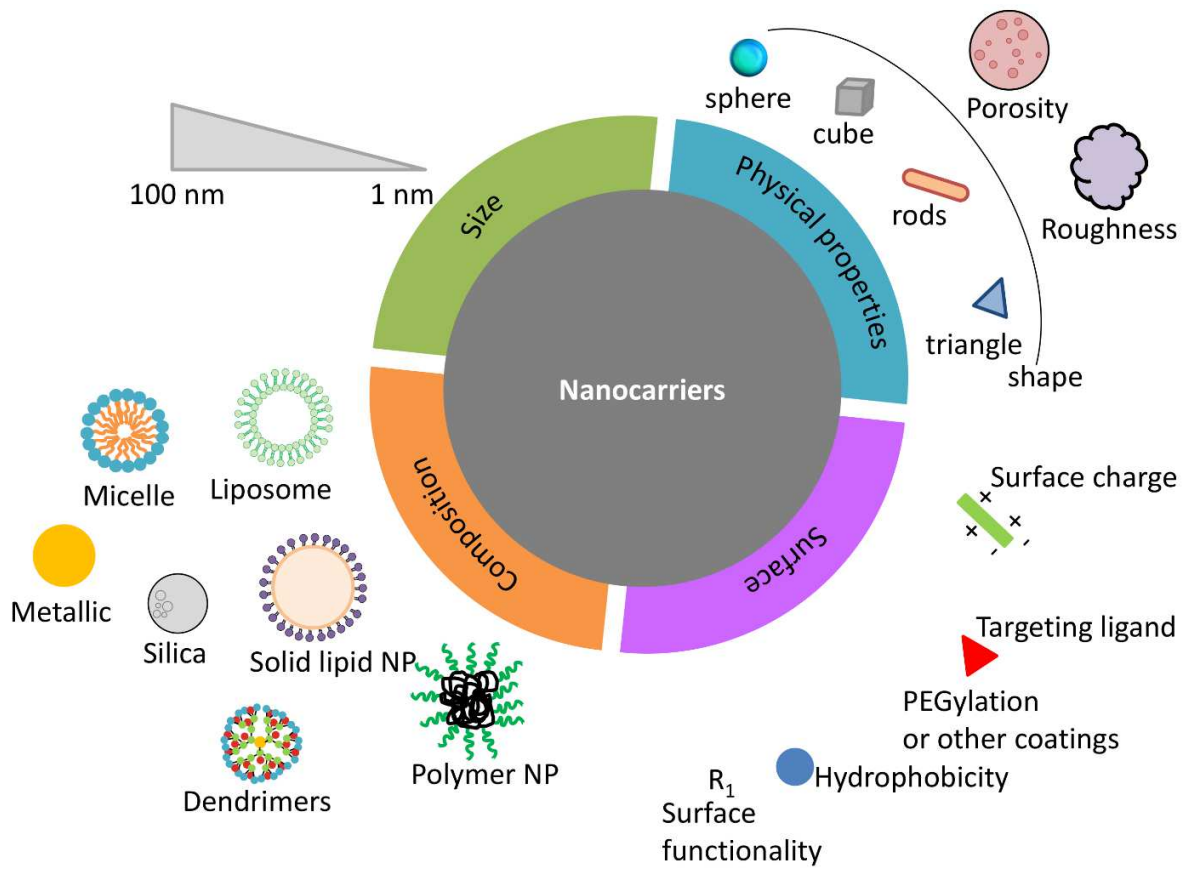
Figure 1. Nanocarriers used in drug delivery. A summary of nanocarriers explored as carriers for drug delivery, together with illustrations of their biophysicochemical properties.
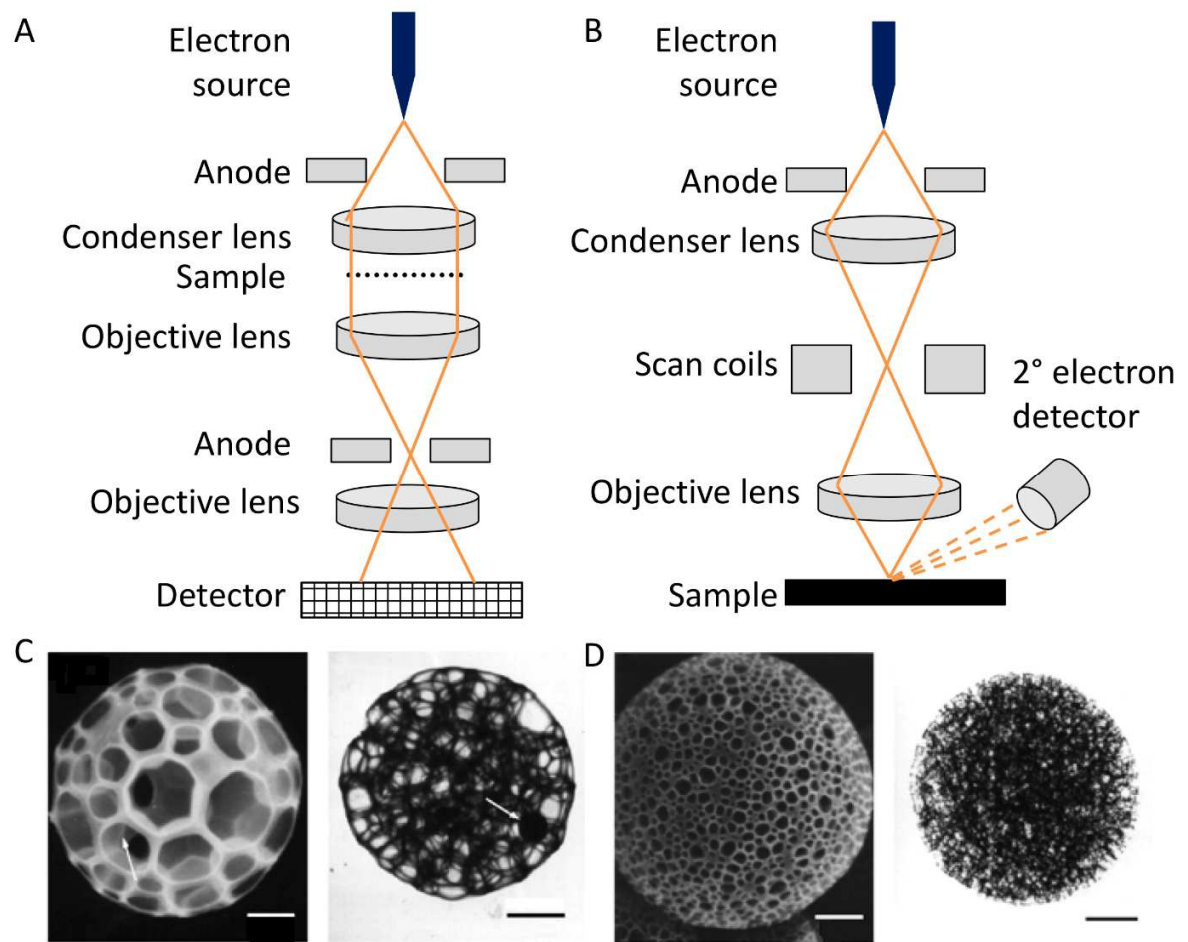
Figure 2. Scanning vs. Transmission electron microscopy. Simplied schematic diagram of A) SEM and B) TEM. C, D) SEM and TEM micrographs of C) poly(methyl methacrylate) (PMMA) microspheres and D) poly(vinyl acetate) (PVA) microspheres prepared under the same conditions. The scale bar = 2 µm.Reproduced from [19] with permission from American Chemical Society.
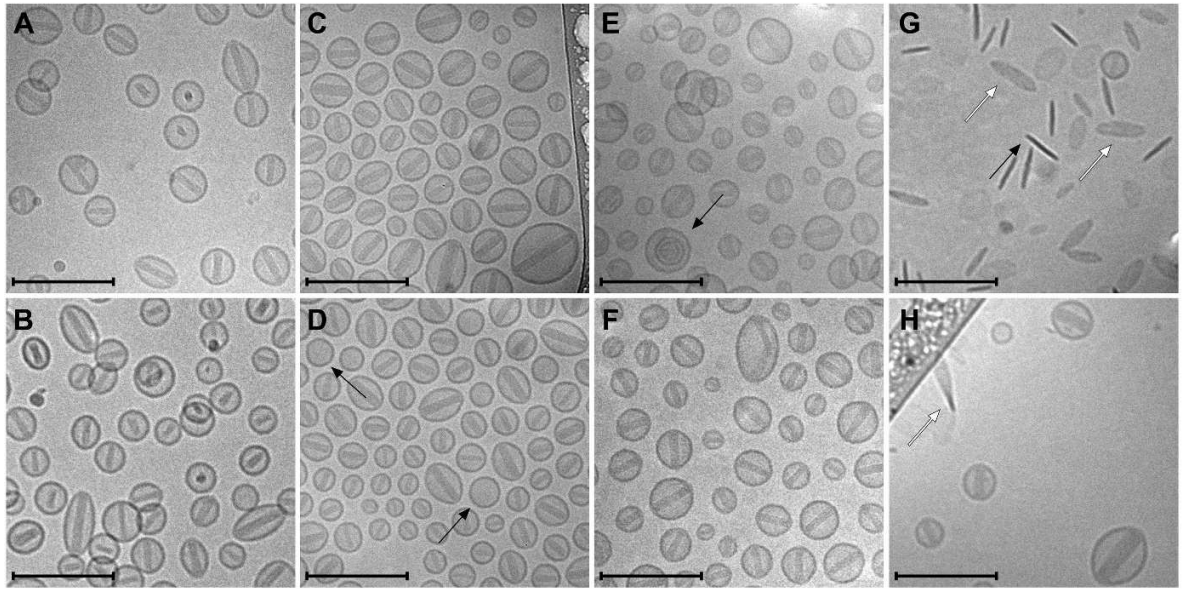
Figure 3. Cryo-TEM analysis of four liposomal doxorubicin formulations. Cryo-TEM images of Doxil® (A, B), Caelyx® (C, D), DOXOrubicin (E, F) and SinaDoxosome (G, H). Scale bars: 200 nm. Black arrows indicate empty liposomes (D), an oligolamellar vesicle (E) and disks (G). White arrows represent face on view of disks (G, H). Reproduced from [26] with permission from Elsevier B.V.
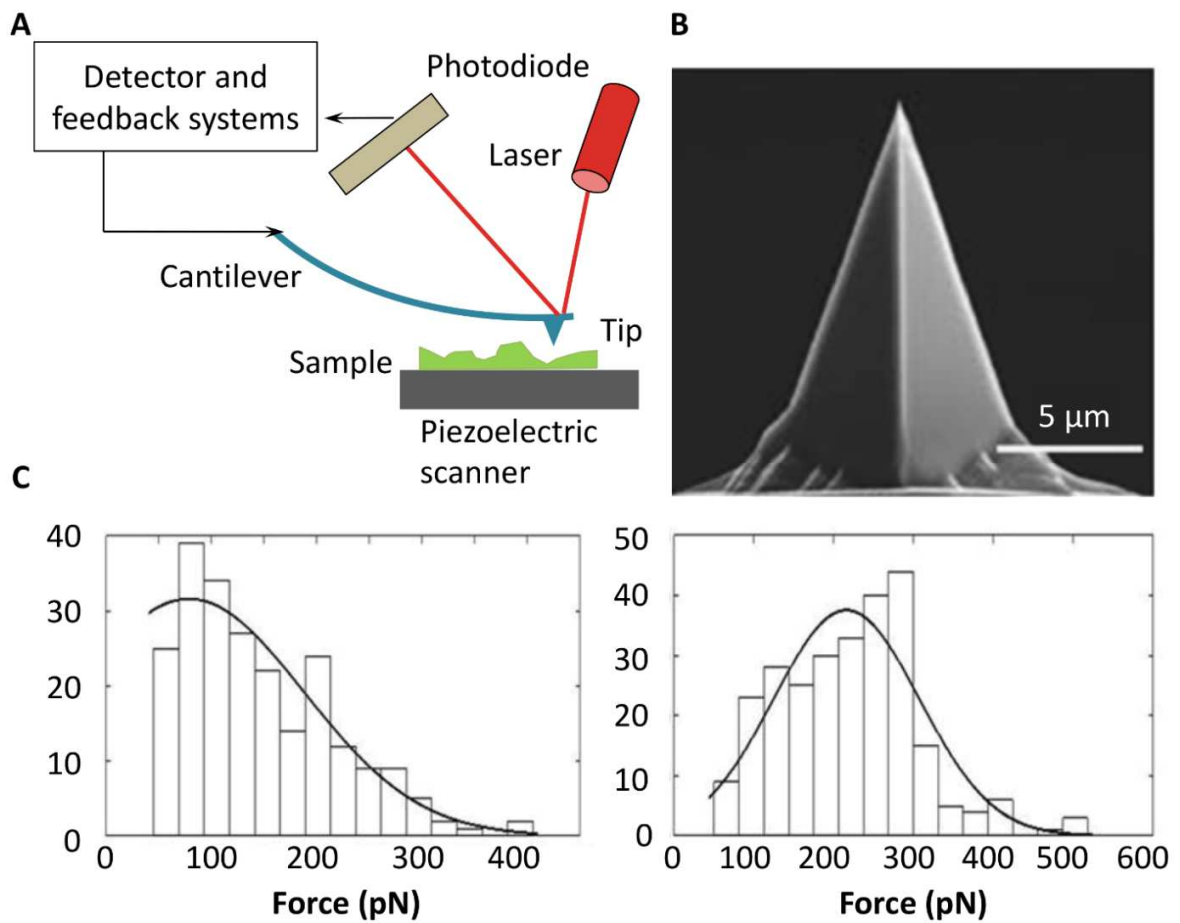
Figure 4. Atomic force microscopy. A) Simplified schematic of AFM. B) SEM micrograph of a AFM probe tip. Reproduced from [32] with permission from AIP publishing. C) Rupture force histogram plotted for substrate functionalized with free folic acid (left) and functionalized with folate decorated nanoparticles (right). Reproduced from [42] with permission from Elsevier B.V.
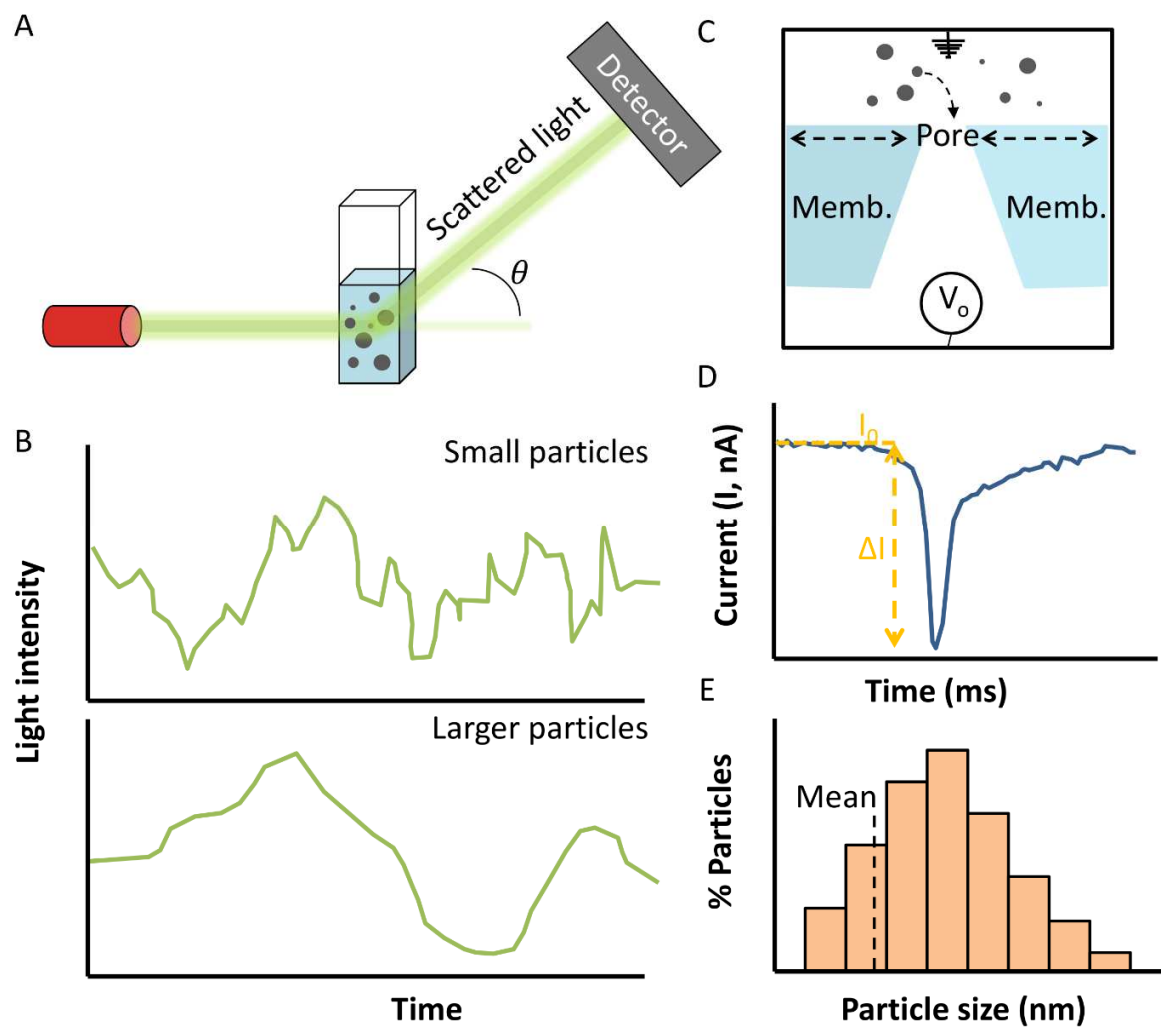
Figure 5. DLS vs. TRPS. A) Schematic illustration of DLS. B) Hypothetical DLS scattering plots of smaller particles (top) and larger particles (bottom). C) Schematic illustration of TRPS. Tunable pores are located in the central septum of a polyurethane membrane (Memb.), placed within a fluid cell. D) Representative data of one typical pulse in detail. E) Number based size distribution obtained from TRPS analysis.
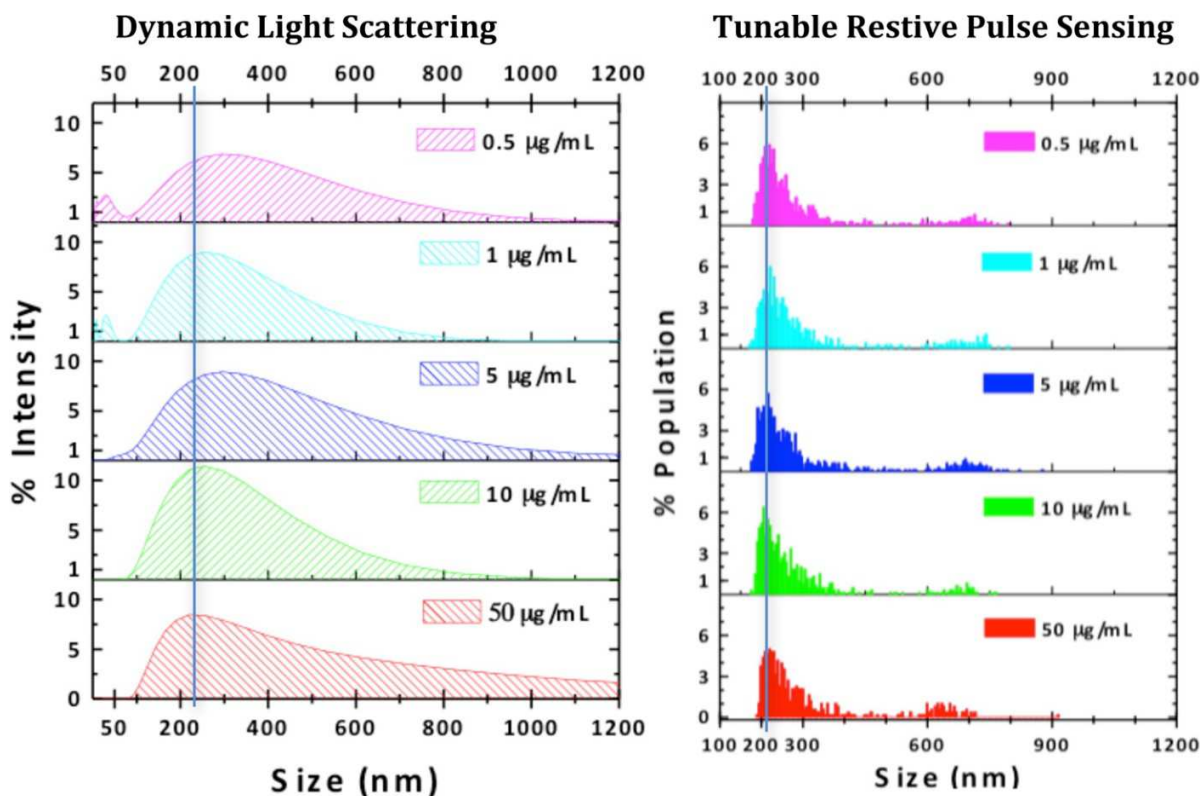
Figure 6. Comparative evaluation of TRPS and DLS in characterizing sensitivity and stability of size distribution measurements of a series of sequential dilutions of nanoparticles from 0.5–50 μg/mL, prepared from a stock solution of 500 μg/mL in RPMI+10% FBS. The graphs represent averages of triplicate measurements. Note changes in the DLS size distributions below 5 μg/mL, especially left-side broadening of the peak and appearance of a smaller peak <50 nm, related to proteins in serum. At higher concentrations (50 μg/mL) the peak broadened to the right. In contrast to DLS, the TRPS size distribution remained fairly constant over the whole concentration range. Reproduced from [61] with permission from Americal Chemical Society.
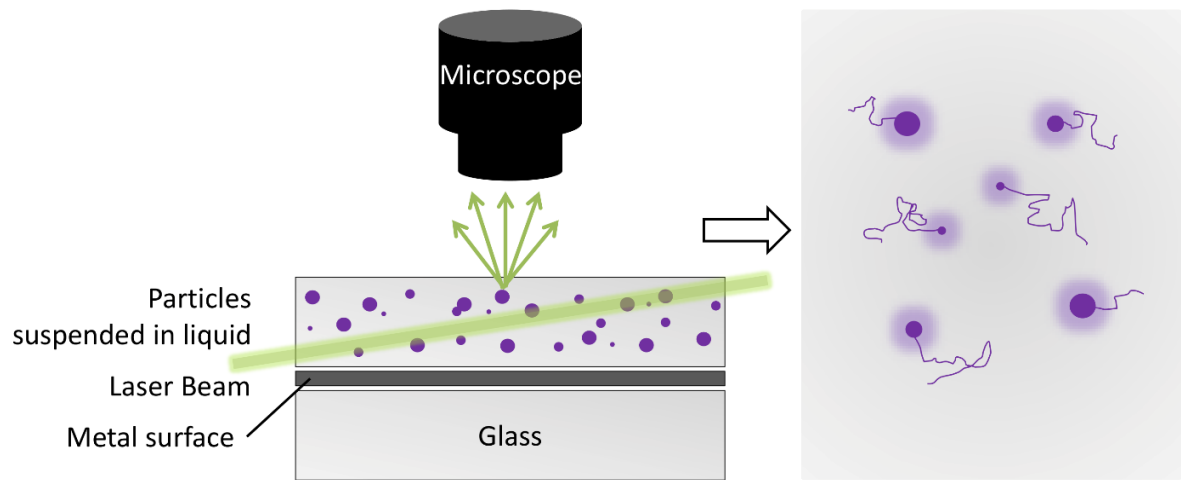
Figure 7. Schematic representation of NTA.
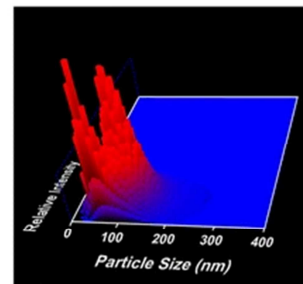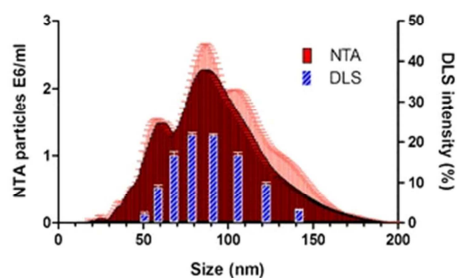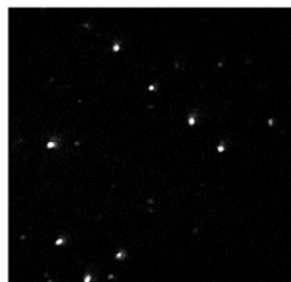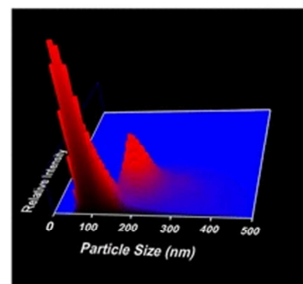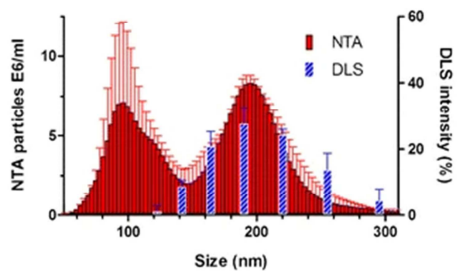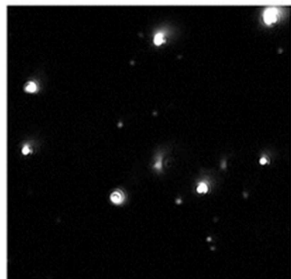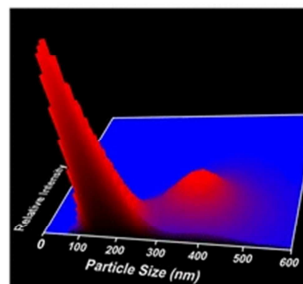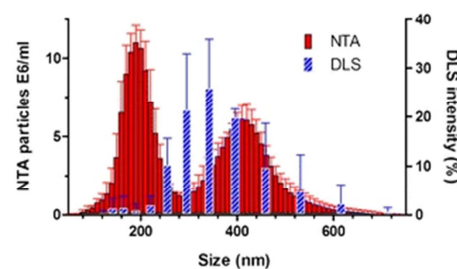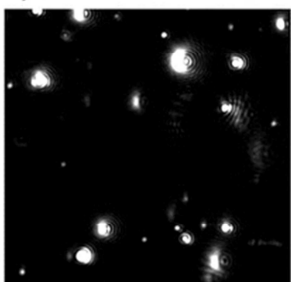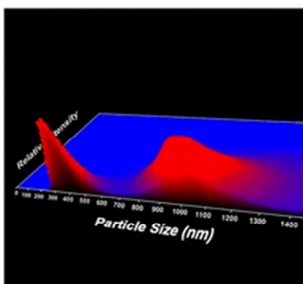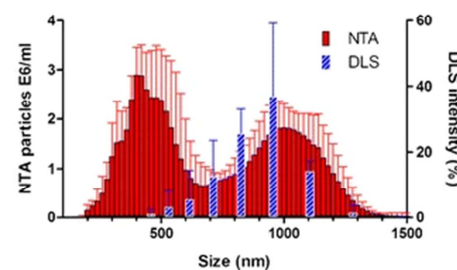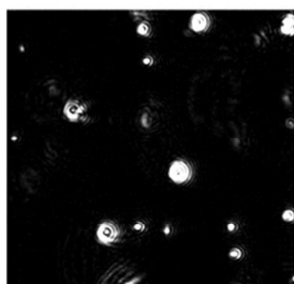
Figure 8. Size distribution from NTA and DLS measurements of mixtures of monodisperse polystyrene beads (middle panels) with the corresponding NTAvideo frame (left panels) and 3D graph (size vs. intensity vs. concentration; right panels). a) 60-nm/100-nm beads at a 4:1 number ratio; b) 100- nm/200-nm beads at a 1:1 number ratio; c) 200-nm/400-nm beads at a 2:1 number ratio; d) 400-nm/1,000-nm beads at a 1:1 number ratio. Reproduced from [62] with permission from American Association of Pharmaceutical Scientists.
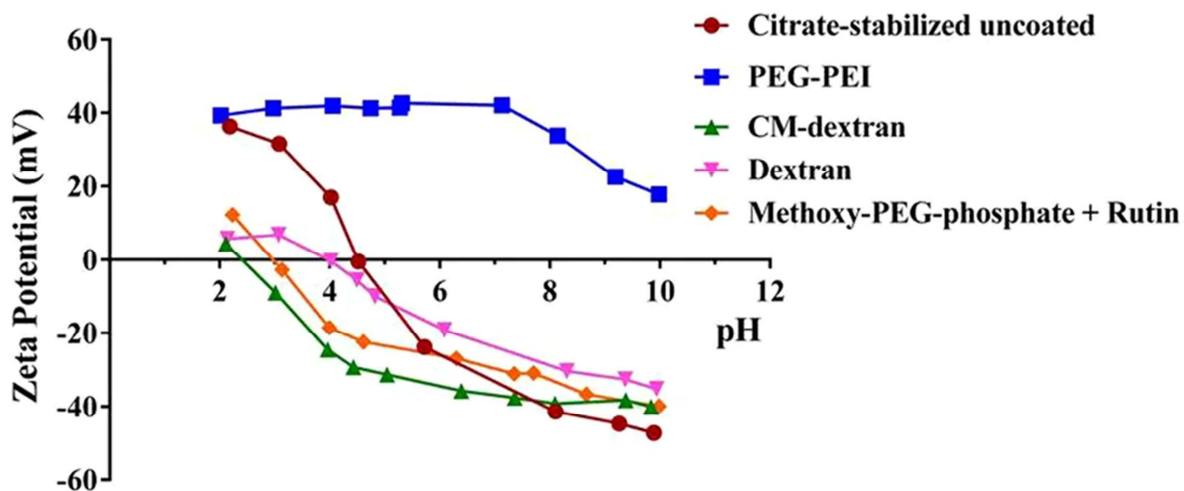
Figure 9. The measured pH-dependent zeta potential of magnetic iron oxide nanoparticles (MNPs) coated with citrate (red), PEG-PEI (blue), CM-dextran (green), dextran (magenta), and methoxy-PEG-phosphate + rutin (amber) in water. All MNP constructs displayed a negative surface charge at pH 7, except PEG-PEI MNPs. Reproduced from [47] with permission from Springer Nature.

Table 1. Effect of dilution on hydrodynamic size by DLS and TRPS

NP dilution in medium	DLS		TRPS	
	$d_{h,z\text{-}ave}$ (nm)	PdI	size mean (nm)	size mode (nm)
1:10	311 ± 11	0.37	317	228
1:50	223 ± 1	0.28	291	204
1:100	240 ± 4	0.48	315	210
1:500	70 ± 2	1	313	223
1:1000	43 ± 2	1	297	208

Table modified from [61]

Table 2. Summary of characterization methods for nanoparticles

Method	Nanoparticle state	Parameter	Advantages	Disadvantages
Transmission electron microscopy (TEM)	High vacuum, dried sample	Size, size distribution Shape	Direct imaging of nanoparticles at very high resolution (<1 nm)	Tedious sample preparation High energy electron beam may damage sample
Scanning electron microscopy (SEM)	High vacuum, low pressure	Size, size distribution, surface structure	Single particle resolution, Lower energy electron beams as TEM	Limited resolution and penetration depth
Atomic force microscopy	Dry or liquid	Size, shape, binding force to modified cantilever	Allows high resolution measurements in different conditions	Particles must adhere to a fixed surface
X-ray diffraction (XRD)	Dry, powdered	Crystallite size	Determines crystalline/amorphous phases and information about crystal structure	Low sensitivity No information about particle size, shape
Small angle X-ray Scattering (SAXS)	Dry, in suspension	Size, size distribution and shape	High sensitivity.	Information about particle morphology is required
Dynamic light scattering	In suspension	Hydrodynamic radius and intensity based size distribution	Large measurement range (0.6 nm to 1µm) Rapid and high throughput	Biased towards larger particles in suspension, difficult data interpretation for polydisperse samples
Tuneable resistive pulse sensing (TRPS)	In suspension (in conductive liquid)	Size, shape, concentration, ζ potential	Tunable detection range, single particle resolution	Requires specific liquid (conductive) and careful initial calibration
Nanoparticle tracking analysis (NTA)	In suspension	Hydrodynamic radius, size distribution, concentration	Single particle resolution, suitable for highly polydisperse samples	Requires highly scattering particles
Laser doppler anemometry (electrophoretic mobility)	In suspension	Surface Charge (ζ-potential)	Rapid and high throughput, minimal sample preparation	Depends on the model applied to convert mobility to ζ potential
Porosimetry	Dry	pore size, pore volume, and surface area of a sample	Compatible with polydisperse samples	Sample cannot be used subsequently